NIH Public Access
Author Manuscript
Phys Med Biol. Author manuscript; available in PMC 2015 January 06.

Published in final edited form as:
Phys Med Biol. 2014 January 6; 59(1): 23–42. doi:10.1088/0031-9155/59/1/23.

Optical artefact characterization and correction in volumetric scintillation dosimetry

Daniel Robertson[1,2], **Cheukkai Hui**[1], **Louis Archambault**[3], **Radhe Mohan**[1,2], and **Sam Beddar**[1,2]

[1] Department of Radiation Physics, The University of Texas MD Anderson Cancer Center, Houston, Texas 77030

[2] The University of Texas Graduate School of Biomedical Sciences at Houston, Houston, Texas 77030

[3] Radiation Oncology, CHUQ Pavillon Hotel-Dieu de Quebec, 11 Cote du Palais, Quebec, QC G1R 2J6 Canada

Abstract

The goals of this study were (1) to characterize the optical artefacts affecting measurement accuracy in a volumetric liquid scintillation detector, and (2) to develop methods to correct for these artefacts. The optical artefacts addressed were photon scattering, refraction, camera perspective, vignetting, lens distortion, the lens point spread function, stray radiation, and noise in the camera. These artefacts were evaluated by theoretical and experimental means, and specific correction strategies were developed for each artefact. The effectiveness of the correction methods was evaluated by comparing raw and corrected images of the scintillation light from proton pencil beams against validated Monte Carlo calculations. Blurring due to the lens and refraction at the scintillator tank-air interface were found to have the largest effect on the measured light distribution, and lens aberrations and vignetting were important primarily at the image edges. Photon scatter in the scintillator was not found to be a significant source of artefacts. The correction methods effectively mitigated the artefacts, increasing the average gamma analysis pass rate from 66% to 98% for gamma criteria of 2% dose difference and 2 mm distance to agreement. We conclude that optical artefacts cause clinically meaningful errors in the measured light distribution, and we have demonstrated effective strategies for correcting these optical artefacts.

1. Introduction

The goal of volumetric scintillation dosimetry is to evaluate the dose distribution of a radiation source by measuring the light emission from a scintillating volume. It was initially proposed and developed for brachytherapy eye plaques (Kirov *et al.*, 2005), and further work has extended its use to photon beams (Ponisch *et al.*, 2009) and proton beams (Fukushima *et al.*, 2006). Recent work has focused on the application of a large-volume liquid scintillator (LS) detector for quality assurance measurements of scanned proton beams (Beddar *et al.*, 2009; Archambault *et al.*, 2012). The detection system used in this study consists of a cubic tank containing a LS solution and a charge-coupled device (CCD) camera for obtaining images of the light distribution in the tank.

In order to accurately measure the scintillation light distribution, one must correct for various optical artefacts that arise as the light propagates from the scintillating centres to the

abeddar@mdanderson.org.

NIH-PA Author Manuscript
NIH-PA Author Manuscript
NIH-PA Author Manuscript

NIH-PA Author Manuscript

NIH-PA Author Manuscript

NIH-PA Author Manuscript

detector and as the detector measures the incident light. Although prior studies have acknowledged the presence of these artefacts and taken initial steps to correct them (Archambault *et al.*, 2012; Ponisch *et al.*, 2009), a systematic evaluation of the impact of optical artefacts and the methods for correcting them has not been performed. The purpose of this study, therefore, was to examine the various sources of optical artefacts present in volumetric scintillation dosimetry and then to develop correction methods to remove or mitigate the effects of those artefacts so that meaningful dosimetric measurements could be obtained. The optical artefacts will be divided into those produced in the scintillator and its container, those associated with the optical train of the camera, and those related to the CCD chip (see Table 1).

1.1. Scintillator tank artefacts

Interactions of scintillation light within the scintillator tank change the light distribution that is measured by the camera and therefore constitute the first source of error to be dealt with by any correction algorithm. Scintillation light undergoes scattering as it travels through the scintillator. In addition, it can be reflected at the tank wall, and its path can be altered by refraction through the window-air interface. Each of these interactions changes the light distribution that is measured by the camera.

Although scintillators are designed to be transparent to their own light emissions, scintillation photons experience Rayleigh scattering and additional scattering due to absorption and re-emission as they pass through the scintillator. The result of this scattering is a blurring of the measured light distribution that is independent of the camera's focus settings. This blurring may be particularly problematic when measuring steep dose gradients and highly heterogeneous radiation fields such as proton Bragg peaks, where blurring leads to a broadening of the Bragg peak and a decrease in its height.

Previous work in volumetric scintillation dosimetry has shown that blurring due to photon scatter can be corrected by deconvolving a point spread function (PSF) from the images (Kirov *et al.*, 2005; Ponisch *et al.*, 2009). These studies obtained the PSF by assuming a functional form of the PSF and then fitting the parameters of the function based on a comparison between the measured and expected scintillation light projections. While this approach provided reasonable results, the PSF was not derived from any measurement or calculation.

Refraction changes the path of light as it travels from one medium to another. Refraction at the interface between the LS solution and the tank window is minimal because the materials' indexes of refraction are similar. However, refraction at the window-air interface is significant, leading to a shift in the expected positions of individual pixels and an increase in the apparent size of objects or light sources within the tank.

Another challenge associated with measuring light from a large volume with a lens-camera system is perspective, the decrease in an object's apparent size with its increasing distance from the lens. Telecentric lenses can be used to acquire images without perspective, but these lenses can only acquire light from an area as large as the diameter of the primary lens. In the case of a large detector such as the one in this study, the weight and cost of a telecentric lens large enough to measure the entire detector would be substantial. If non-telecentric optics are used for quantitative measurements, the size of objects must be scaled by their distance from the lens.

NIH-PA Author Manuscript

NIH-PA Author Manuscript

NIH-PA Author Manuscript

1.2. Optical train artefacts

The scintillation light from the detector is collected and transmitted to the CCD chip by a compound optical lens, which introduces additional artefacts, including vignetting, lens distortion, and blurring due to the point spread function of the lens.

Vignetting is the decrease in a camera's measurement efficiency with distance from the image centre, and is typically classified as mechanical, optical, or natural. Mechanical and optical vignetting are caused by the physical obstruction of light in the optical train and can be prevented by appropriate selection of the lens settings. Natural vignetting is caused by the divergence of light as it travels from the lens to the image sensor. The degree of natural vignetting varies with the lens and camera design, but it is present in most cameras and must be corrected for accurate quantitative light measurement over the entire image.

Lens distortion is the nonlinear mapping of radial distance in image space that results from imperfect lens design. It is typically either ‘barrel distortion,’ in which the image is magnified at the centre relative to the edges, or ‘pincushion distortion,’ in which the image is magnified at the edges relative to the centre. Modern scientific lenses are designed to minimize lens distortion, but no lens is perfect.

In addition to the blurring caused by light scattering in the scintillating medium, the lens itself also introduces blurring to the optical system. As a result, the blurring in the scintillator detector is a combination of two PSFs, one from scattering in the scintillator and one from the lens.

1.3. CCD artefacts

The CCD chip is the final source of error in the image acquisition chain. CCD chips are subject to various sources of noise, including photon noise, dark noise, and readout noise An additional source of noise is stray radiation, including gamma rays and secondary neutrons, protons, and nuclear fragments. The CCD can be exposed to these stray particles, which may deposit their energy within individual pixels, leading to transient spikes or streaks in the images.

2. Materials and methods

The detection system used in this study was described previously (Archambault *et al.*, 2012). Here, we will describe the details of the system that are relevant for consideration of the optical artefacts. We will then describe our methods for characterizing and correcting the optical artefacts of interest. The correction methods will be addressed in the order in which they are applied in the image processing chain. The image processing workflow (Fig. 1) proceeds in reverse order of the photon path, beginning at the CCD and concluding with refraction and blurring in the scintillator tank. With the exception of the Monte Carlo dose calculations, all computations and analysis were performed using MATLAB version 2012b (The MathWorks, Natick, MA).

2.1. Liquid scintillator detector

The detection system used in this study consists of a cubic tank containing a volume of LS solution, with a CCD camera for measuring the light distribution in the tank (Fig. 2). The LS solution serves as the detection medium and also as the attenuating phantom. The LS solution used in this study is BC-531 (Saint-Gobain Crystals, Hiram, OH), which consists of scintillating molecules in a mixed solvent of linear alkyl benzene and 1,2,4-trimethylbenzene. The density of the scintillator is 0.87 g cm^{-3}, and its refractive index is 1.47. Its light emission peak is centred at 425 nm, its light output is 59% of the output of

NIH-PA Author Manuscript

NIH-PA Author Manuscript

NIH-PA Author Manuscript

anthracene, and the decay time of the principal scintillation light emission is 3.5 ns. A scintillator-to-water proton range scaling factor of 0.902 was calculated for BC-531 using the Monte Carlo package MCNPX version 2.7.0 (Los Alamos National Laboratory, Los Alamos, CA).

The tank walls are made of opaque polyvinyl chloride (PVC), except for one wall, which is made of clear polymethyl methacrylate (PMMA). This PMMA wall serves as a window through which the camera views the light emission from the scintillator. The tank and camera are connected by a light-tight housing, also constructed of PVC, which isolates the detector optics from ambient light. The tank dimensions are 20×20×20 cm^3, and the camera is located 70 cm away from the tank. To reduce reflections from the grey PVC tank walls, the interior walls of the tank were covered with a lining of black polymer. The surface of this polymer was roughened by hand with sandpaper to further reduce reflections. Reflections at the LS-air interface at the top of the tank were avoided by filling the tank until the LS-air interface was above the region viewed by the camera.

The CCD camera used in this study is the Luca^{EM} S 658M (Andor Technology, Belfast, Northern Ireland). The CCD resolution is 658×496 pixels, and the physical pixel size is 10 μm. The camera digitizes optical signals at 14 bits and is capable of measuring 37 full frames per second. The chip is cooled to −20°C via an on-board thermoelectric cooling system. An objective lens (JML Optical Industries, Rochester, NY) with an effective focal length of 25 mm was fitted to the camera, and the focus and aperture were set to 0.82 m and f/5.6, respectively, resulting in a focal depth of 11.6 cm centred on the scintillator tank.

2.2. Artefact analysis and correction methods

2.2.1. CCD artefacts

CCD noise: Dark frame images were acquired to measure the dark current and noise of the CCD camera. Dark frame images were obtained by taking repeated images with the lens cover attached. Because the temperature of the CCD chip affects the dark current and noise, all images in this study were obtained after the CCD temperature had stabilized at its set point of −20° C. To evaluate the effect of exposure time on the dark noise, we took a series of dark frames with exposure times ranging from 4.7×10^{-4} s (the minimum exposure time available on the camera) to 100 s. The average pixel value and the standard deviation of the pixel values over the entire image were calculated as a function of exposure time. In practice, the offset due to dark current is subtracted during background subtraction. However, the noise in the dark current remains along with the other CCD noise sources.

Stray radiation: The transient spikes and streaks in the CCD images caused by stray radiation were removed by applying a spatial median filter. While a temporal median filter is preferred for spatial accuracy, temporal filters require at least three repeated acquisitions of any given field. To avoid this repetition, we applied a spatial median filter to the 3×3 region surrounding each pixel.

2.2.2. Lens artefacts

Vignetting: Natural vignetting is approximated by the '$\cos^4(\theta)$ law of illumination' (Ray, 1994), which states that the degree of vignetting is proportional to $\cos^4(\theta)$, where θ is the angle between the optical axis and the ray from the exit pupil of the lens to the measurement point on the imaging sensor (Fig. 3). The vignetting value for a given pixel *(i,j)* can therefore be calculated by the equation

NIH-PA Author Manuscript

NIH-PA Author Manuscript

NIH-PA Author Manuscript

$$V_{i,j}=cos^4(\theta_{i,j})=\frac{a^4}{\left(a^2+d_{i,j}^2\right)^2} \quad (1)$$

Where a is the distance from the exit pupil to the principal point (the point where the optical axis meets the image sensor), and $d_{i,j}$ is the distance from the principal point to pixel (i,j). Depending on the lens design, the distance a may differ significantly from the focal length. In the event that the parameter a is not known, it can be approximated by the ratio of the object-space focal distance to the measured object-space pixel size at the focal plane. The $\cos^4(\theta)$ rule is only strictly valid for thin lenses, and some commercially available lenses diverge significantly from this behaviour (Goldman, 2010). However, the $\cos^4(\theta)$ rule provides a simple analytical model of vignetting that is effective in many cases. Those desiring a more accurate vignetting correction can use alternate vignetting models, such as those proposed by Litvinov and Schechner (2005) or Goldman (2010).

The vignetting in our lens-camera system was measured by analysing flat field images. These were acquired by attaching a diffusing filter to the front of the lens and acquiring images of the centre of a flat screen computer monitor at close range. Several flat field measurements with different camera orientations were averaged together to reduce the impact of any non-uniformities in the monitor output. The resulting flat field was fit to a $\cos^4(\theta)$ function using least squares optimization. The pixel size of the camera was known, allowing $d_{i,j}$ to be calculated precisely. Because the distance a was not known for the lens used in this study, the fit of the $\cos^4(\theta)$ function consisted of fitting the parameter a of equation 1. The vignetting in the detector system was corrected by scaling each image by the $\cos^4(\theta)$ function determined by the fit.

Lens distortion: One approach to solving the lens distortion problem is to calibrate a lens and map its distortion modes. Camera calibration methods using vanishing points and vanishing lines to identify the camera focal length have been extensively developed (Caprile and Torre, 1990; Wang and Tsai, 1990), and calibration techniques for determining lens distortion have been developed for machine vision applications (Tsai, 1992; Zhang, 1999). In this study, lens distortions were measured and corrected using the Camera Calibration Toolbox for Matlab (Bouguet, 2010), which is an implementation of the previously cited camera calibration techniques. It was used to develop a model of the camera's intrinsic and extrinsic parameters, including focal length, principal point, and lens distortions, based on multiple images of a checkerboard pattern at different orientations. The lens distortion was modelled using the second order symmetric radial distortion model used by Zhang (1999). The calibrated distortion model then was used to restore the rectilinearity of each image acquired with the detector.

Lens PSF: In the simplifying case of a perfect (aberration-free) lens, the PSF is produced by the diffraction of light from the source as it travels through the lens aperture, and is equivalent to the Fraunhofer diffraction pattern of the aperture. Real lenses diverge from this ideal behaviour, as the PSF is broadened by imperfections in the optical system.

The point spread function of a lens with a fixed focal length can be described as a function of six variables, including the wavelength of the light, the image coordinates (x and y), the lens aperture, the distance from the lens to the object (z), and the back focal distance (Shih *et al.*, 2012). In the case of the detector described here, the light wavelength, lens aperture, and back focal distance are fixed. This leaves the lens-object distance and the image coordinates as the variable parameters of the PSF. Because the lens-object distance is constrained to the

NIH-PA Author Manuscript

NIH-PA Author Manuscript

NIH-PA Author Manuscript

inside of the scintillator tank, the lens PSF is essentially a three-dimensional function with a unique value for every point in space within the scintillator tank.

The PSF of the entire system consists of the convolution of the lens PSF and the PSF due to light scatter within the scintillator:

$$PSF_{sys}(x,y,z) = PSF_{scatter}(x,y,z) * PSF_{lens}(x,y,z) \quad (3)$$

While PSF_{lens} is technically a function of the three-dimensional location inside the scintillator tank, in practice its variation may be small enough over the region of interest that an invariant PSF_{lens} could be assumed as a first-order approximation. Because of the expected small variation and the difficulty of measuring the PSF_{lens} at multiple locations, we assumed an invariant PSF_{lens} in this study. We leave as future work the determination of the spatial variation of PSF_{lens}.

PSF_{lens} was measured using the method described in ISO standard 12233 for measuring the resolution of photographic cameras (ISO, 2000). This process involves three steps:

1. Photograph a slanted edge formed by the interface between black and white regions.
2. Measure the edge-spread function (ESF) perpendicular to the slanted line. Repeating this measurement at multiple locations along the slanted line allows the ESF to be determined with a resolution greater than the camera resolution.
3. Take the derivative of the ESF to obtain the line-spread function, which is the one-dimensional equivalent of the PSF.

The test pattern was formed by joining a black strip of plastic to a white strip along a carefully machined straight edge. This pattern provided the required ESF and was chemically compatible with the scintillator solution. This test pattern was affixed to a rigid surface and viewed at an angle with the camera to produce the requisite slanted edge. The measurement of PSF_{lens} in air was compared to the measurement of PSF_{sys} performed in the scintillator tank, as described in section 2.2.3.

2.2.3. Scintillator tank artefacts

Refraction and perspective: Refraction and image perspective both affect the location and apparent size of objects and light sources within the tank. Because of this interconnection, refraction and perspective are corrected simultaneously. We developed a first-order correction for refraction and perspective based on the simplifying assumption that our camera system is a pin-hole camera. As shown in Fig. 4a, any photon created along the line $\overline{MC}$ is projected onto the point X in the camera focal plane. Therefore, the apparent size and location of an object depends on its distance away from the focal plane. The presence of the scintillator solution creates an additional change in the object's apparent size and location. As shown in Fig. 4b, refraction changes the direction of the photon track and thus changes the observed position of the photon origin. In addition to change of location, the change in apparent pixel size causes a change in the pixel value in the CCD image.

Refraction and perspective are corrected analytically based on the pin-hole camera assumption. The index of refraction of the LS is 1.47 and that of the acrylic tank is 1.49. Since refraction at the LS-window interface is very small, only refraction at the window-air interface is considered in the correction. Considering that most of the photons are created along the proton track, the goal of the correction is to translate the image from the focal plane to the plane of the proton track.

NIH-PA Author Manuscript

NIH-PA Author Manuscript

NIH-PA Author Manuscript

First, the coordinate of each pixel in the camera plane is mapped to the proton track plane using Snell's law and trigonometric identities. Based on the coordinate translation map, the ratio of the pixel area at the proton track plane to that at the focal plane is calculated for each pixel. The pixel value at the proton track plane is then normalized by dividing each pixel value by its corresponding area ratio. For example, if the area ratio is smaller than 1, the normalized pixel value will be higher than the measured value. The normalized pixel values with the translated coordinates are then used to interpolate to the final pixel value at the proton track plane.

Photon scatter: The final step of our artefact correction is to address photon scatter in the scintillator. We adapted the method described in section 2.2.2 to measure PSF_{sys} for the scintillation detector. The test pattern was placed in the scintillator tank, and the light source for the photograph was produced by exciting the scintillator with an ultraviolet lamp (F15T8/BLB, General Electric Lighting) with a 368-nm emission peak. This ensured that the wavelength of light used for the measurement was the same as that of the light produced during LS irradiation. The PSF_{sys} measurement was repeated with the test pattern placed at a distance of 3 cm, 10 cm, and 16 cm from the tank window in order to evaluate the relationship between scatter and the distance travelled through the scintillator.

The low-intensity tail of the measured PSF was fit to an exponential function. This preserved the shape of the PSF and prevented the noise in its low-intensity tail from propagating to the images during blurring correction. Blurring in the detector was corrected by deconvolving the measured PSF from the detector images using the Lucy-Richardson deconvolution algorithm (Biggs and Andrews, 1997).

2.3 Artefact correction evaluation methods

For each source of error, our goal was to describe the magnitude of error it caused and the effectiveness of our correction method for mitigating it. Thereafter, we used gamma analysis to identify the correction steps that played the greatest role in restoring the images to the original dose distributions.

Proton pencil beams of four energies (85.6, 100.9, 144.9, and 161.6 MeV) were used for in-depth testing of the optical artefact corrections. Depth-light profiles were plotted for qualitative comparison of the measured and calculated distributions. The overall effectiveness of the optical artefact corrections was evaluated by comparing raw and corrected CCD measurements with Monte Carlo dose calculations.

Two-dimensional gamma analysis (Low *et al.*, 1998) was performed to quantify the agreement between the CCD images and the corresponding projections of the Monte Carlo dose distributions. The analysis included all pixels in which the reference distribution was at least 5% of the maximum value. This analysis was performed with the uncorrected and corrected images and with each one of the corrections left out to show its contribution to the overall correction process.

Gamma analysis was also performed on the corrected images with the analysis parameters varying from 1% to 3% dose difference and from 1 mm to 3 mm distance to agreement. Beginning at the commonly used gamma analysis criteria of 3% dose difference and 3 mm distance to agreement, we decreased both of these parameters until the passing rate for at least one of the beam energies dipped below 95%, which we set as the limit for ‘acceptable agreement’ between the measured and calculated distributions.

While it is common practice to use a percentage of the maximum dose as the dose difference criterion for gamma analysis, we elected to use a percentage of the local dose at each pixel

NIH-PA Author Manuscript

NIH-PA Author Manuscript

NIH-PA Author Manuscript

as the dose difference criterion. We consider this to be appropriate for this study because the maximum dose in a proton Bragg peak is much higher than the average dose in the region, and the use of a percentage of the maximum dose would be too generous of a dose difference criterion, limiting the utility of gamma analysis for comparison of dose distributions.

2.3.1. Proton beam measurements—Proton beam measurements with the scintillator detector were carried out at the MD Anderson Cancer Center Proton Therapy Center–Houston on the scanning beam gantry. The detector was aligned isocentrically on the treatment couch, and mono-energetic proton pencil beams were directed into the scintillator tank perpendicular to the camera axis at a depth of 10 cm from the tank window. Pencil beams were also delivered at depths of 5 cm and 15 cm from the tank window in order to evaluate the variation in light scatter with distance travelled through the scintillator. The experimental setup is shown in Fig. 5. Nominal proton beams of the four energies named above were delivered and measured separately. A total of 220 monitor units, as described in Gillin *et al.* (2010), was delivered for each beam energy. The CCD camera acquired images at 2 frames per second, so that each proton beam was delivered over the course of 2 images.

2.3.2. Monte Carlo calculations—Three-dimensional (3D) dose distributions were calculated for the beam energies named above using the Monte Carlo radiation transport code MCNPX, version 2.7d (Waters *et al.*, 2002) with validated phase space models of the specific scanning beam nozzle being used (Sawakuchi *et al.*, 2010). The voxel size was set to 1 mm perpendicular to the beam direction, and it varied from 1 mm to 0.1 mm in the beam direction, with higher resolution in the steep-dose-gradient region around the Bragg peak.

Scintillators exhibit a non-linear response to ionizing radiation with varying linear energy transfer, a phenomenon called ionization quenching. This phenomenon causes an under-response of the scintillator in the Bragg peak because of the steep increase in linear energy transfer in the Bragg peak region. To account for this effect in the comparison between the Monte Carlo and CCD data, we applied a quenching model to the Monte Carlo dose data to obtain the scintillating radiation output. The parameters for this model were determined in a previous study by our group for the same detector configuration (Robertson *et al.*, 2013).

3. Results

We will first describe the magnitudes of the individual sources of error and their correction methods. Following this, we will give the results of the gamma analysis to identify the correction steps that played the greatest role in restoring the images to the original dose distributions.

3.1. CCD artefacts

3.1.1 CCD noise—The dark current of the CCD camera was evaluated by calculating the mean pixel value and standard deviation over the entire frame for a range of exposure times (Fig. 6). As expected, the dark noise increased linearly with time. This is illustrated by a linear fit to the data, with an R^2 value of 0.9992. The baseline dark signal pixel value for the CCD is 510. The dark current offset is corrected during background subtraction.

3.1.2. Stray radiation—The spatial median filter effectively removed single-pixel spikes caused by stray radiation (Fig. 7). The mean number of transient spikes and streaks in the test images decreased from 3 to 0 after the median filter was applied. The median filter did not significantly affect the shape of the underlying light distribution.

NIH-PA Author Manuscript

NIH-PA Author Manuscript

NIH-PA Author Manuscript

3.2. Lens artefacts

3.2.1 Vignetting—The $\cos^4(\theta)$ vignetting model provided a good approximation to the measured vignetting behaviour of the camera (Fig. 8).The fit to equation 1 yielded a value of a = 26.5 mm, which matches well with the lens focal length of 25 mm and the approximation of a based on object-space parameters, which was 26.9 mm. While the $\cos^4(\theta)$ model did not perfectly match the measured signal falloff, the agreement is considered sufficient for the purposes of this study. The under-response due to vignetting measured for this detector was as great as 4% at the corners of the image, with 7.8% of all pixels under-responding by 3% or more. After the vignetting correction was applied, 99.8% of pixels in the flat field image were within 1% of the pixel value at the centre of the image.

3.2.2. Lens distortion—As expected, the lens distortion model obtained from the calibration process showed very little distortion in the centre of the field of view. Pixels at the edges of the field of view could be displaced by as much as 2 pixels, which corresponds to a measurement error of 0.6 mm (Fig. 9). The small magnitude of these distortions illustrates the quality and appropriateness of the lens selected for this detector.

Lens PSF: The PSF_{lens} measurement results are described in conjunction with the PSF_{sys} measurement results in section 3.3.2.

3.3.Scintillator tank artefacts

3.3.1. Refraction and perspective—The average increase in apparent pixel size due to refraction was 4.1% at the focal plane. The expansion of pixel size caused a relative decrease in pixel count. The apparent pixel count reduction was 7.7% at the image centre and 7.8% in the corners. Both of these effects were corrected. Since our proton track was aligned with the focal plane, no additional step was needed to refocus the track to a different plane.

3.3.2. Photon scatter—PSF_{sys} was found to be a sharp peak with very steep fall-off, dropping to 0.015% within 10 pixels from the centre. At a distance of 8 pixels from the centre, the noise contribution was significant enough that, while the PSF continued to decrease on average, it no longer decreased monotonically. In order to extend the range of the measured PSF beyond 8 pixels, the low-intensity tail was fit to a decreasing exponential function. This allowed the measured PSF to be extrapolated to a distance of 64 pixels from the centre.

To our surprise, there was no substantial difference between the PSF_{sys} measurements performed at different depths in the scintillator. In addition, the measured PSF_{lens} was equivalent to the measured PSF_{sys} (Fig. 10). This suggests that PSF_{lens} is the primary contributor to PSF_{sys} in our detector, with $PSF_{scatter}$ making a negligible contribution. The invariance of PSF_{sys} with depth in the scintillator tank is confirmed by comparison of the lateral profiles of proton pencil beams delivered at depths of 5, 10, and 15 cm from the tank window. After correction for perspective, attenuation, and inverse-square intensity falloff, there was no substantial difference between the profiles (Fig. 11).

3.4. Artefact correction evaluation

The corrected CCD light distribution on the beam's central axis exhibited a clear improvement in agreement with the Monte Carlo light distribution in comparison to the uncorrected CCD light distribution (Fig. 12). The light distributions all exhibited decreased signal in the Bragg peak due to quenching, as described in section 2.3.2.

NIH-PA Author Manuscript

NIH-PA Author Manuscript

NIH-PA Author Manuscript

Gamma analysis was used to compare the scintillation light measurements from the LS detector system with the projected scintillation light distributions calculated using Monte Carlo methods. The minimum gamma analysis parameters that provided 'acceptable agreement' were 2%/2 mm and 3%/1 mm. The gamma analysis pass rates for the varying gamma criteria are given in Table 2 for each of the four beam energies. The gamma pass maps with the 2% and 2 mm criteria are shown in Fig. 13 for the 85.6-MeV and 144.9-MeV proton beams.

The gamma analysis clearly demonstrates the effectiveness of the optical artefact corrections applied to the CCD data. With the common gamma criteria of 3%/3 mm, the average passing rate rose from 85.6% for the uncorrected light distributions to 99.7% for the corrected distributions. Using the more stringent criteria of 2%/2 mm, the difference was larger, rising from 65.9% for the uncorrected distribution (Fig. 13, top) to 98.2% for the corrected distribution (Fig. 13, bottom) on average.

To evaluate the contribution of each step in the overall correction process, the gamma analysis was repeated with each of the corrections omitted. The results are shown in Table 3. The contribution of the spatial median filter, vignetting, and lens distortion corrections was minimal. The refraction correction was larger, and the greatest proportion of the overall correction was contributed by the blurring correction.

4. Discussion

4.1. Point spread function

We determined that blurring from the lens was the primary source of the overall PSF, while light scatter in the scintillator was negligible. This was contrary to our expectations, as previous studies assumed that light scatter was the primary source of blurring. This result suggests that the scintillator BC-531 effectively meets the desirable criteria of transparency to its own emissions. It also highlights the importance of using high-quality optics in order to obtain the narrowest possible PSF.

While unexpected, this finding is fortuitous, as it renders unnecessary the use of different PSFs for different depths within the scintillator tank. While photon scatter proved to be insignificant in this study, we wish to emphasize that this result is valid only for the scintillator BC-531, and that the level of scattering in other scintillators has not yet been evaluated for this application. The primary significance of this finding is that blurring due to the lens is non-negligible and requires separate treatment from blurring due to light scatter.

4.2. Gamma analysis

In our results, the areas that most frequently failed the gamma analysis were the low-dose edges, where noise and offsets in the background level have a much larger influence than they do on the beam axis. This is a result of our decision to use a percentage of the local pixel dose in our gamma analysis rather than a percentage of the maximum dose, as is commonly used in radiation therapy dose evaluation. The local dose difference is a stricter criterion, which provides more meaningful comparisons in low-dose regions. Had we chosen to use a percentage of the maximum dose, the pixels in these low-dose areas would have passed.

The vignetting and lens distortion corrections showed little contribution to the gamma pass rate in this study, and in some cases they even caused a small decrease in the passing rate. However, the value of these corrections should not be overlooked. The vignetting and lens distortion corrections are largest at the edges of the image, and because our dose distributions included very little data near the image edges, these corrections appeared to

NIH-PA Author Manuscript

NIH-PA Author Manuscript

NIH-PA Author Manuscript

have little effect. That being said, the use of low-distortion lenses and telecentric lenses could render lens distortion and vignetting corrections unnecessary, especially considering that the data at the tank edges are likely to be less important than the data in the centre.

The spatial median filter had a small negative effect on the gamma pass rates. This is unsurprising given the tendency of median filters to blur sharp edges. However, this effect was small, and gamma analysis is not sensitive to the spikes and streaks that the median filter is designed to remove. The median filter may prove to be more important when multiple cameras are used to obtain a 3D reconstruction of the light distribution, as high-intensity spikes could interfere with 3D reconstruction algorithms.

4.3. Sources of error

The central-axis light signal data shown in Fig. 12 reveal an imperfect match between the Monte Carlo calculations and the corrected CCD data. The disagreements may come from several possible factors, including noise in the CCD measurements as well as imperfections in the correction factors and Monte Carlo calculations. The refraction and perspective corrections only apply analytically to one plane within the detector, and the light signal outside of that plane cannot be completely corrected for these phenomena. However, we believe that in the current study, this limitation was not observed because the dose was concentrated along a single narrow pencil beam.

The most notable disagreement between the CCD and Monte Carlo data was in the maximum light intensity at the Bragg peak, which differed by ±3%. This variation was unsurprising, given the sharpness of the proton Bragg peak and the high spatial resolution of the data. An additional source of error in the Bragg peak height came from the quenching parameters applied to the Monte Carlo dose calculations to obtain the Monte Carlo light distribution. In a previous study, we reported that this quenching calculation method was accurate to within ±5% (Robertson *et al.*, 2013), and the maximum errors in that study were in the Bragg peak. This source of uncertainty alone is sufficient to explain the deviations between the Monte Carlo and CCD peak light values. Further efforts to decrease the error in the quenching correction process are underway.

An additional source of error in the correction factors is the difficulty of exactly measuring the PSF. Our method allowed us to measure the PSF with twice the spatial resolution of the CCD camera, but this resolution was still coarse compared to the sharp peak of the PSF. We selected the peak value of the PSF by fitting a Gaussian function to the immediately surrounding data points, but this method only provides an approximate peak value. The actual peak value may vary by as much as a factor of 2, which could change the results of the blurring correction. However, our results match the Monte Carlo data well, suggesting that our measured PSF was sufficiently close to the actual PSF to provide an accurate blurring correction for this detector system. An alternative approach for analytically calculating the lens PSF based on the lens prescription (Shih *et al.*, 2012) may provide improvements in accuracy while also facilitating the use of a PSF that varies with position inside the tank.

4.4. Reflections

Reflection of the scintillation light is a source of artefacts that was not dealt with directly in this study. Reflections may occur at any interface between the scintillator and the tank wall, the tank window, or the air above the scintillator. Reflections have been problematic in previous studies involving volumetric scintillation dosimetry (Beddar *et al.*, 2009; Ponisch *et al.*, 2009; Kirov *et al.*, 2005). Reflections are highly dependent on the geometry and materials of the scintillator tank, and are difficult to correct through image processing. We

NIH-PA Author Manuscript

NIH-PA Author Manuscript

NIH-PA Author Manuscript

believe that the best approach to minimize artefacts due to reflection is to prevent them through careful detector design, such as we did in the steps described in section 2.1.

5. Conclusions

Optical artefacts introduce significant deviations into the scintillation light distribution measured by the described volumetric scintillation detector. Optical artefact corrections are essential to accurately measure the intensity and spatial distribution of the scintillation light emission.

The largest optical artefacts in this detector system are blurring due to the lens PSF and refraction at the tank window-air interface. Blurring can be corrected very effectively by deconvolution of the PSF, which can be directly measured using the process described above. Refraction can be analytically modelled and corrected because of the simple geometry of the detector system. Photon scatter in the scintillator was not found to be a significant source of artefacts.

Other optical artefacts that introduce detectable deviations to the measured light signal include vignetting, lens distortion, and the spikes and streaks caused by stray radiation incident on the CCD chip. These artefacts can be corrected through camera calibration and image filtering, but the correction steps may be unnecessary, depending on the prevalence of stray radiation in the vicinity of the camera and the quality and type of optical components.

Using the described correction methods, we have demonstrated gamma analysis passing rates of 95% or higher with the criteria of 2% local dose difference and 2 mm distance to agreement, when comparing corrected images from the scintillation detector to dose distributions calculated using Monte Carlo methods. We conclude that optical artefacts must be addressed in order to obtain accurate light measurements, and we have demonstrated effective strategies for correcting these optical artefacts. The optical artefact correction methods described here can be directly applied to future systems incorporating multiple cameras to facilitate a full 3D reconstruction of the light signal.

Acknowledgments

The project described was supported in part by award number P01CA021239 from the National Cancer Institute. The content is solely the responsibility of the authors and does not necessarily represent the official views of the National Cancer Institute or the National Institutes of Health. This research was performed in partial fulfilment of the requirements for the PhD degree from The University of Texas Graduate School of Biomedical Sciences at Houston.

References

Archambault L, Poenisch F, Sahoo N, Robertson D, Lee A, Gillin M T, Mohan R, Beddar S. Verification of proton range, position, and intensity in IMPT with a 3D liquid scintillator detector system. Med. Phys. 2012; 39:1239–46. [PubMed: 22380355]

Beddar S, Archambault L, Sahoo N, Poenisch F, Chen GT, Gillin MT, Mohan R. Exploration of the potential of liquid scintillators for real-time 3D dosimetry of intensity modulated proton beams. Med. Phys. 2009; 36:1736–43. [PubMed: 19544791]

Biggs DSC, Andrews M. Acceleration of iterative image restoration algorithms. Appl. Opt. 1997; 36:1766–75. [PubMed: 18250863]

Bouguet, J-Y. Camera Calibration Toolbox for Matlab. California Institute of Technology; Pasadena, CA: 2010.

Caprile B, Torre V. Using vanishing points for camera calibration. Int. J. Comput. Vision. 1990; 4:127–39.

NIH-PA Author Manuscript

NIH-PA Author Manuscript

NIH-PA Author Manuscript

Fukushima Y, Hamada M, Nishio T, Maruyama K. Development of an easy-to-handle range measurement tool using a plastic scintillator for proton beam therapy. Phys. Med. Biol. 2006; 51:5927–36. [PubMed: 17068374]

Gillin MT, Sahoo N, Bues M, Ciangaru G, Sawakuchi G, Poenisch F, Arjomandy B, Martin C, Titt U, Suzuki K, Smith AR, Zhu XR. Commissioning of the discrete spot scanning proton beam delivery system at the University of Texas MD Anderson Cancer Center, Proton Therapy Center, Houston. Med. Phys. 2010; 37:154–63. [PubMed: 20175477]

Goldman DB. Vignette and Exposure Calibration and Compensation. IEEE Trans. Pattern Analysis and Machine Intelligence. 2010; 32:2276–88.

ISO. ISO 12233: Photography -- Electronic still-picture cameras -- Resolution measurements. International Organization for Standardization; Geneva, Switzerland: 2000.

Kirov AS, Piao JZ, Mathur NK, Miller TR, Devic S, Trichter S, Zaider M, Soares CG, LoSasso T. The three-dimensional scintillation dosimetry method: test for a Ru-106 eye plaque applicator. Phys. Med. Biol. 2005; 50:3063–81. [PubMed: 15972981]

Litvinov A, Schechner YY. Radiometric framework for image mosaicking. 2005; 22:839–48.

Low DA, Harms WB, Mutic S, Purdy JA. A technique for the quantitative evaluation of dose distributions. Med. Phys. 1998; 25:656–61. [PubMed: 9608475]

Ponisch F, Archambault L, Briere TM, Sahoo N, Mohan R, Beddar S, Gillin MT. Liquid scintillator for 2D dosimetry for high-energy photon beams. Med. Phys. 2009; 36:1478–85. [PubMed: 19544763]

Ray, SF. Applied Photographic Optics: Lenses and Optical Systems for Photography, Film, Video, and Electronic Imaging. Focal Press; Woburn, MA: 1994.

Robertson D, Mirkovic D, Sahoo N, Beddar S. Quenching correction for volumetric scintillation dosimetry of proton beams. Phys. Med. Biol. 2013; 58:261–73. [PubMed: 23257200]

Sawakuchi GO, Mirkovic D, Perles LA, Sahoo N, Zhu XR, Ciangaru G, Suzuki K, Gillin MT, Mohan R, Titt U. An MCNPX Monte Carlo model of a discrete spot scanning proton beam therapy nozzle. Med. Phys. 2010; 37:4960–70. [PubMed: 20964215]

Shih, Y.; Guenter, B.; Joshi, N. Image Enhancement Using Calibrated Lens Simulations. In: Fitzgibbon, A., et al., editors. Computer Vision – ECCV 2012. Springer Berlin Heidelberg; 2012. p. 42-56.

Tsai, RY. A versatile camera calibration technique for high-accuracy 3D machine vision metrology using off-the-shelf TV cameras and lenses. In: Wolff, LB.; Shafer, SA.; Healey, G., editors. Radiometry. Jones and Bartlett Publishers, Inc.; Burlington, MA: 1992. p. 221-44.

Wang LL, Tsai WH. Computing camera parameters using vanishing-line information from a rectangular parallelepiped. Machine Vision and Applications. 1990; 3:129–41.

Waters, LS.; Hendricks, J.; McKinney, G. Monte Carlo N-Particle Transport Code system for Multiparticle and High Energy Applications. Los Alamos National Laboratory; Los Alamos, NM: 2002.

Zhang Z. Flexible camera calibration by viewing a plane from unknown orientations. Computer Vision, 1999. The Proceedings of the Seventh IEEE International Conference on. 1999; 1:666–73.

NIH-PA Author Manuscript

NIH-PA Author Manuscript

NIH-PA Author Manuscript

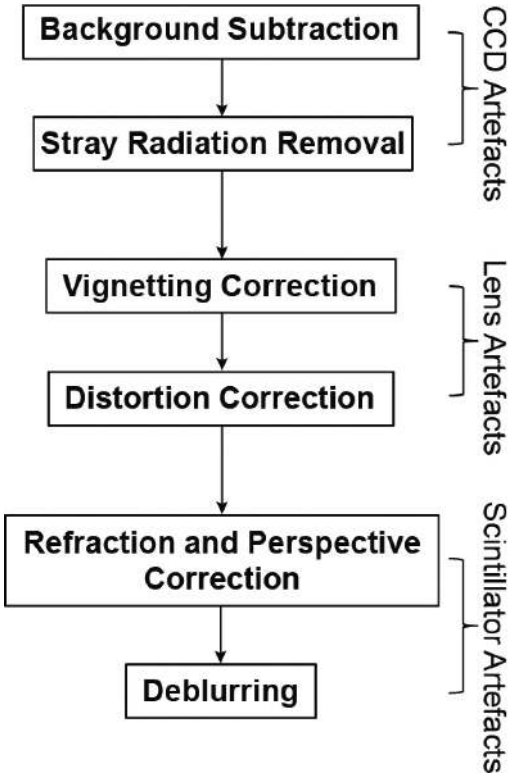

Figure 1.
Workflow of the optical artefact correction process.

NIH-PA Author Manuscript
NIH-PA Author Manuscript
NIH-PA Author Manuscript

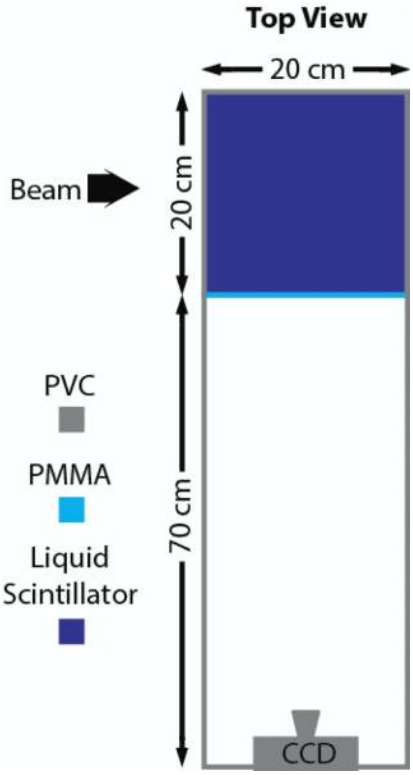

Figure 2.
Liquid scintillator detector system.

NIH-PA Author Manuscript

NIH-PA Author Manuscript

NIH-PA Author Manuscript

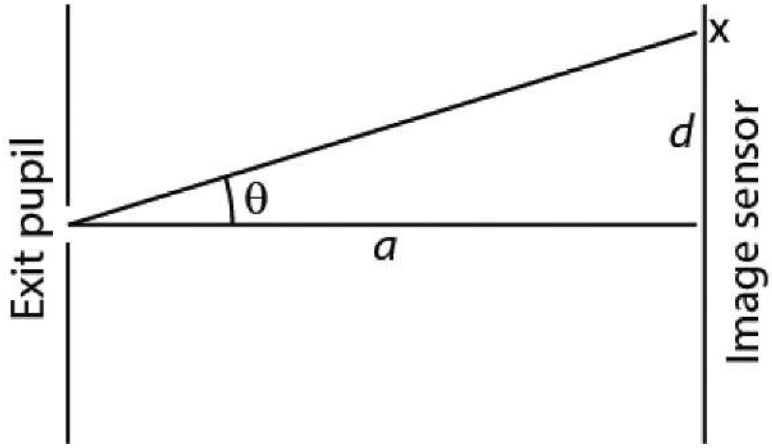

Figure 3.
The angle used in the '$\cos^4\theta$ rule' for camera vignetting is defined as the angle between the camera's optical axis and the ray from the exit pupil of the lens to measurement point *x* on the image sensor.

NIH-PA Author Manuscript

NIH-PA Author Manuscript

NIH-PA Author Manuscript

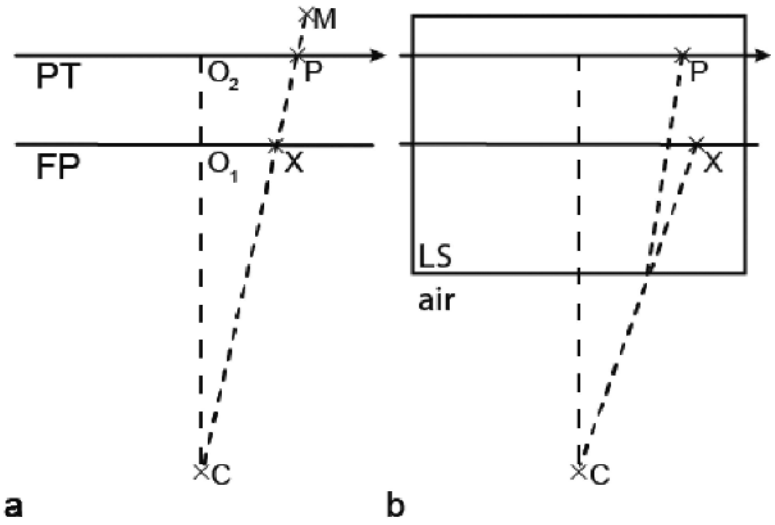

Figure 4.

Consider a pinhole camera located at point C. a) The camera is focused on the focal plane (FP) where $\overline{O_1C}$ **is the focal length. Photons originating from line** $\overline{MC}$ will be translated to the point X in the FP in the CCD image. For example, point P of the proton track (PT) will be mapped to point X at the FP. The apparent location of P will be shortened from $\overline{O_2P}$ **to** $\overline{O_1X}$ in the FP. b) In the presence of the liquid scintillator (LS), the photon beam is bent at the LS-air junction, causing another displacement of apparent location to a different point the FP. The correction algorithm calculates the mapping from X back to P. In addition, it corrects the pixel values altered by the change in apparent pixel size.

NIH-PA Author Manuscript

NIH-PA Author Manuscript

NIH-PA Author Manuscript

Figure 5.
Experimental setup for proton beam measurements with the scintillator detector.

NIH-PA Author Manuscript

NIH-PA Author Manuscript

NIH-PA Author Manuscript

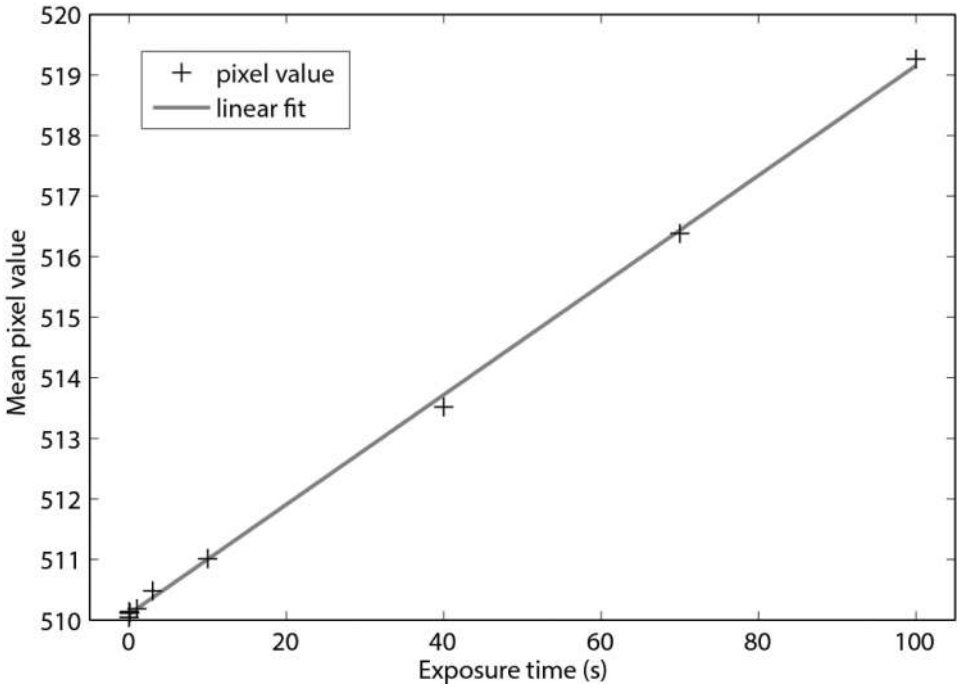

Figure 6.
The mean pixel value of the CCD for dark frame images of various exposure lengths.

NIH-PA Author Manuscript

NIH-PA Author Manuscript

NIH-PA Author Manuscript

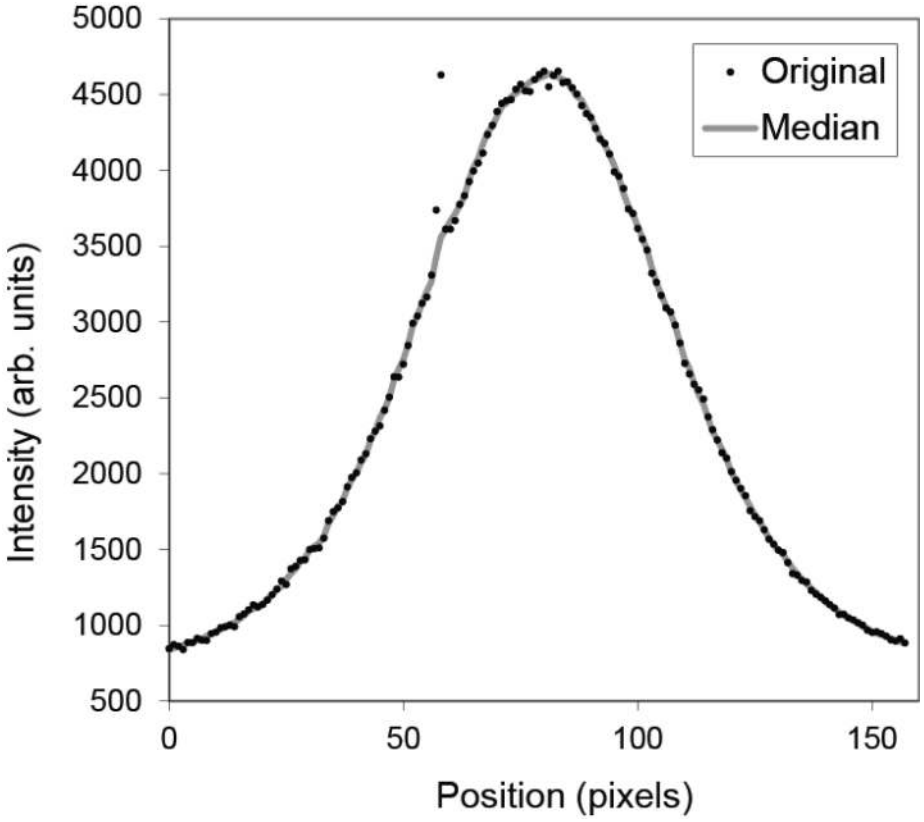

Figure 7.
The lateral profile of a 100.9-MeV proton pencil beam before (black) and after (grey) application of a 3×3 spatial median filter. The median filter effectively removed the transient spike caused by stray radiation incident on the CCD chip without affecting the underlying light distribution.

NIH-PA Author Manuscript
NIH-PA Author Manuscript
NIH-PA Author Manuscript

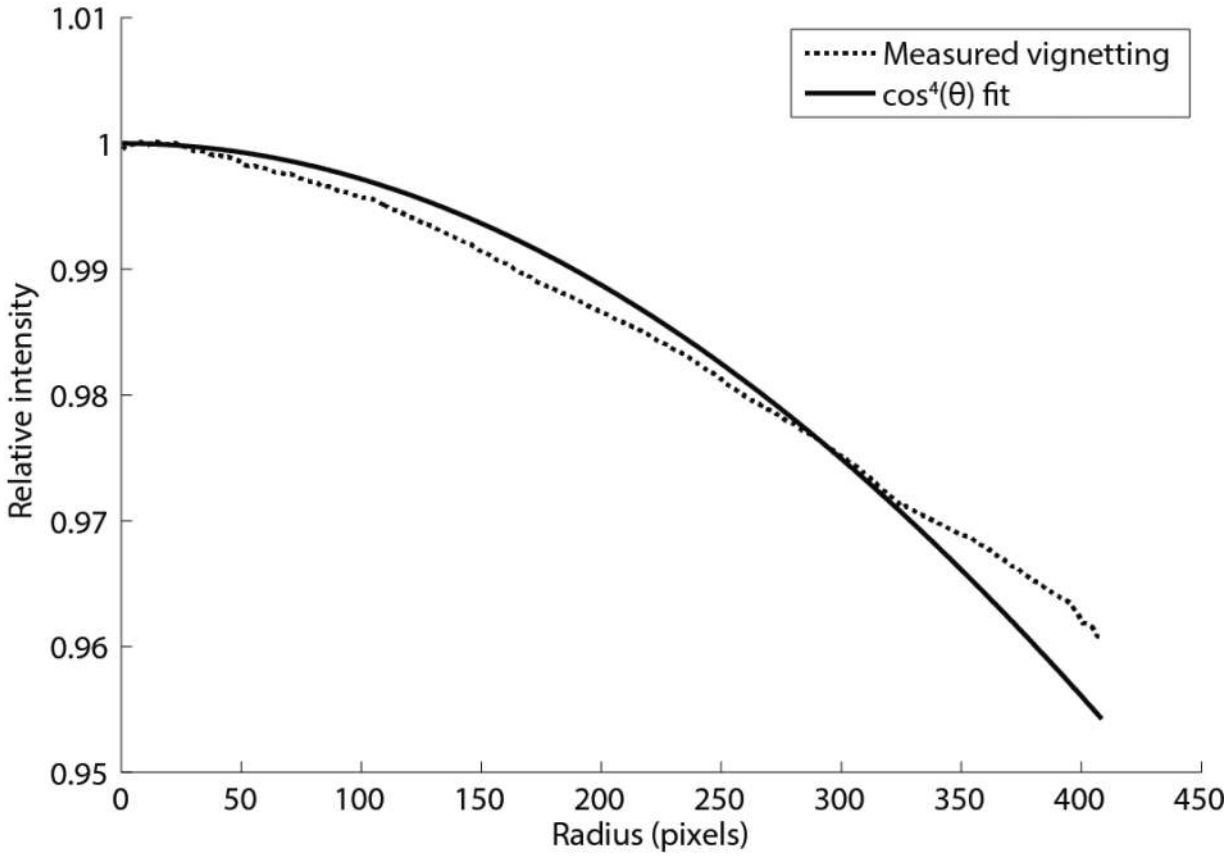

Figure 8.
The measured vignetting as a function of distance from the lens centre (dashed line) is compared to the $\cos^4(\theta)$ function (solid line) used to model the vignetting.

NIH-PA Author Manuscript

NIH-PA Author Manuscript

NIH-PA Author Manuscript

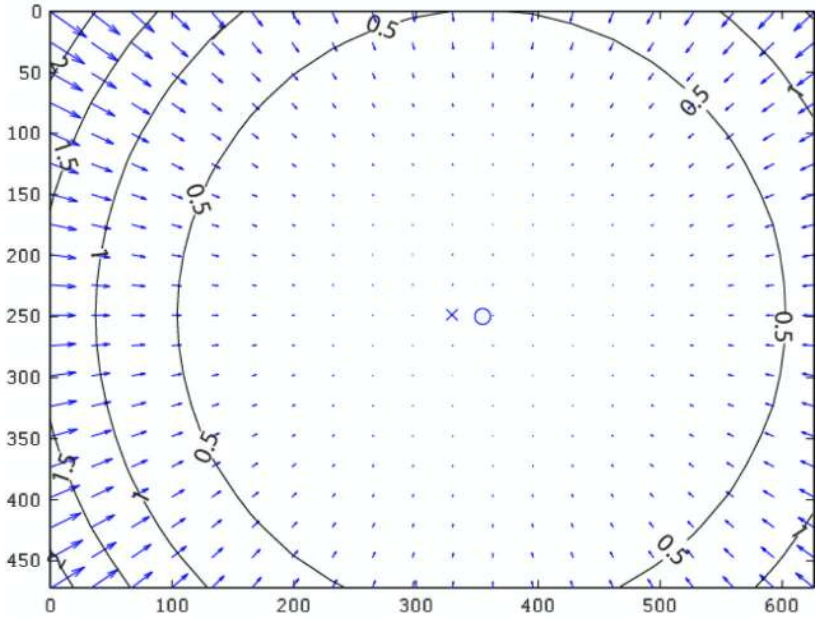

Figure 9.

The lens distortion model of the CCD camera. The direction and magnitude of the arrows indicate the direction and relative magnitude of the pixel position corrections. The contour plot indicates the magnitude of pixel position corrections in units of pixels. The '×' indicates the image centre, and the '○' marks the principal point of the camera.

NIH-PA Author Manuscript

NIH-PA Author Manuscript

NIH-PA Author Manuscript

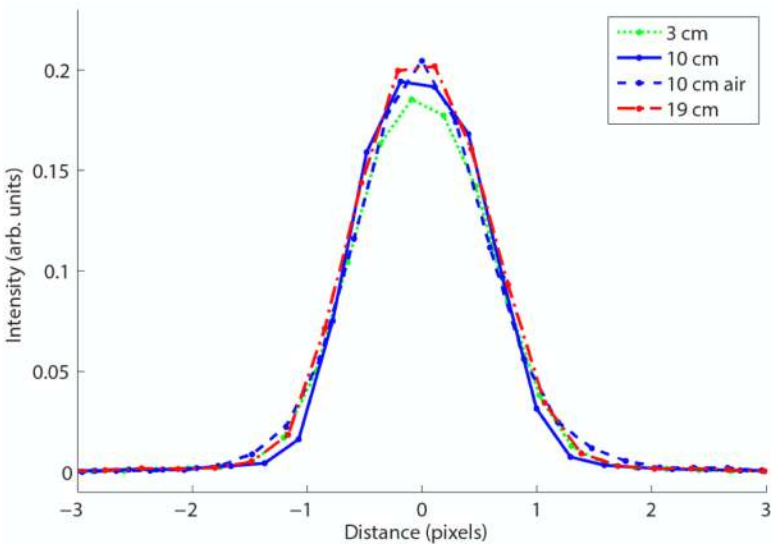

Figure 10.
The PSF of the scintillator detector, measured at a distance of 3 cm (green), 10 cm (blue), and 19 cm (red) behind the tank window, and the PSF of the lens measured in air at a distance equivalent to 10 cm behind the tank window (blue dashed).

NIH-PA Author Manuscript

NIH-PA Author Manuscript

NIH-PA Author Manuscript

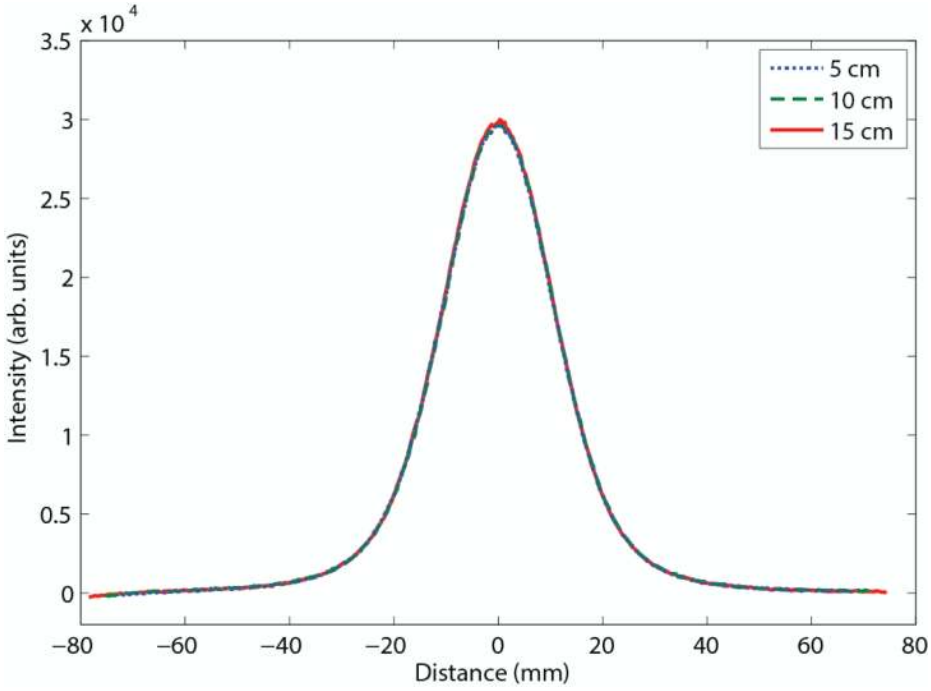

Figure 11.
The lateral profile at the Bragg peak of a 144.9 MeV proton pencil beam, delivered at a distance of 5 cm (blue), 10 cm (green), and 15 cm (red) behind the tank window.

NIH-PA Author Manuscript

NIH-PA Author Manuscript

NIH-PA Author Manuscript

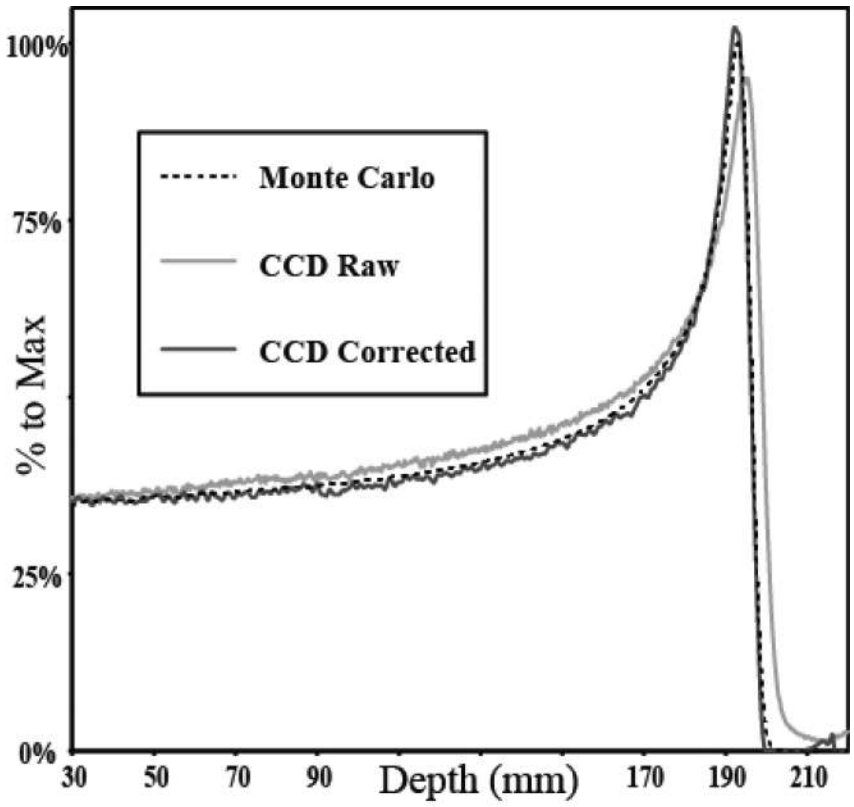

Figure 12.
Central-axis comparison of light signals from Monte Carlo calculations (dashed line) and the raw (gray) and corrected (black) CCD images.

NIH-PA Author Manuscript

NIH-PA Author Manuscript

NIH-PA Author Manuscript

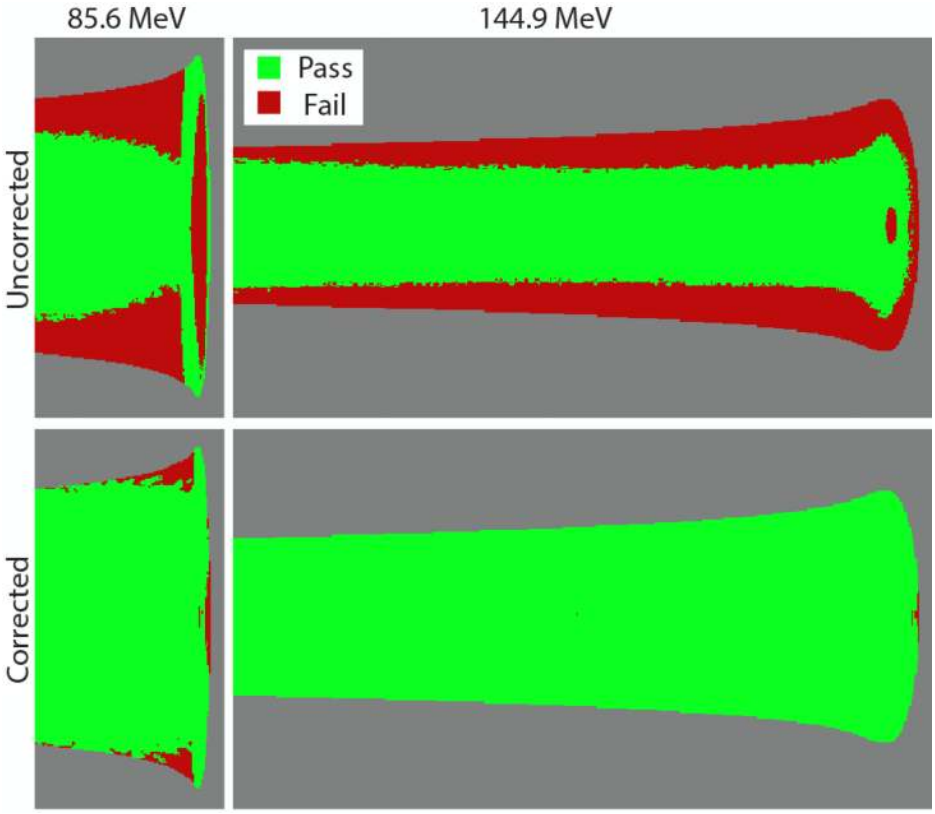

Figure 13.

Gamma analysis pass maps with gamma criteria of 2% and 2mm for 85.6-MeV (left) and 144.9-MeV (right) proton pencil beams. Passing pixels are in red, and failing pixels are in green. The blue pixels are below the dose threshold (5% of maximum dose) and were not considered in the gamma analysis. Top) Uncorrected CCD images. Bottom) Corrected CCD images.

NIH-PA Author Manuscript

NIH-PA Author Manuscript

NIH-PA Author Manuscript

Table 1

Optical artefacts in a volumetric scintillation dosimetry system.

Artefact source	Physical phenomenon	Effect
Light propagation in the scintillator and tank	Photon scattering	Blurring of light signal
	Refraction	Changes in effective pixel size and intensity
	Perspective	Changes in effective pixel size with depth
Optical train	Vignetting	Decreased brightness at image periphery
	Lens distortion	Radial variation in pixel size and location
	Lens point spread function	Blurring of light signal
CCD chip	Stray radiation	Hot pixels and streaks
	Background noise	Measurement uncertainty and pixel value offset

NIH-PA Author Manuscript

NIH-PA Author Manuscript

NIH-PA Author Manuscript

Table 2

Gamma analysis pass rates for proton pencil beam light distributions measured with the scintillator detector, as compared to projected dose distributions calculated using Monte Carlo methods.

Gamma Criteria	Gamma Analysis Pass Rates							
	85.6 MeV		100.9 MeV		144.9 MeV		161.6 MeV	
	Original	Corrected	Original	Corrected	Original	Corrected	Original	Corrected
3%, 3 mm	80.7%	99.1%	81.9%	99.7%	84.5%	100.0%	95.3%	100.0%
2%, 3 mm	80.3%	98.9%	81.5%	99.7%	84.0%	100.0%	94.9%	99.9%
1%, 3 mm	79.3%	98.7%	80.6%	99.6%	82.8%	99.7%	94.1%	99.8%
3%, 2 mm	61.2%	95.3%	63.5%	98.4%	65.3%	99.9%	76.2%	99.9%
2%, 2 mm	60.6%	94.9%	62.9%	98.3%	64.6%	99.9%	75.5%	99.8%
1%, 2 mm	59.4%	93.9%	61.6%	98.0%	63.4%	99.5%	74.0%	99.4%
3%, 1 mm	31.8%	76.9%	31.7%	85.1%	37.7%	97.8%	43.9%	99.7%

NIH-PA Author Manuscript

NIH-PA Author Manuscript

NIH-PA Author Manuscript

Table 3

Differences in gamma analysis (2%, 2 mm) pass rates for measured CCD images lacking one of the optical artefact correction steps, as compared to projected dose distributions calculated using Monte Carlo methods. The comparison was performed for four beam energies.

	Difference in Pass Rates			
Post-processing	**85.6 MeV**	**100.9 MeV**	**144.9 MeV**	**161.6 MeV**
No correction	−34.8%	−35.6%	−35.3%	−24.4%
w/o median filter	0.4%	0.1%	0.0%	0.0%
w/o vignetting	0.0%	−0.4%	0.0%	0.0%
w/o lens distortion	0.9%	0.1%	−0.1%	0.0%
w/o refraction	−26.4%	−12.5%	−1.5%	−3.5%
w/o de-blurring	−18.4%	−19.6%	−20.8%	−7.5%